# Employing surface curvature for spatially resolved X-ray reflectivity: graphene domains on liquid copper

Valentina Belova, Maciej Jankowski, Mehdi Saedi, Irene M. N. Groot, Gilles Renaud, Oleg V. Konovalov

ADVANCED MATERIALS INTERFACES
Open Access
www.advmatinterfaces.de

# Employing Surface Curvature for Spatially Resolved X-Ray Reflectivity: Graphene Domains on Liquid Copper

*Valentina Belova,* Maciej Jankowski, Mehdi Saedi, Irene M. N. Groot, Gilles Renaud, and Oleg V. Konovalov**

**Here the possibility of utilizing X-ray reflectivity for visualization with ≈µm spatial resolution of a surface with a heterogeneous electron density due to a partial coverage by another nanometrically thin material is demonstrated. It requires the sample to be convexly bent, thus reflecting the collimated incident beam onto a magnified image recorded by a position-sensitive detector. By the use of a small, intense, and parallel beam such as provided by the most recent synchrotron sources, one can record such spatially resolved X-ray reflectivity with 0.1–1 kHz frame rate. The use of the method for in situ, time-resolved characterization of single-layer graphene domains during their chemical vapor deposition on a naturally curved surface of a liquid copper drop is demonstrated. This method can follow the growth kinetics, including the coverage ratio, 2D crystal (flake) sizes, and distances between flakes. By taking a single scan, the individual X-ray reflectivity curves can be reconstructed, of both covered and noncovered parts of the surface, allowing to deduce the corresponding electron density profiles perpendicular to the surface. The technique has a promising perspective for in situ study of 2D materials, ultrathin films, and self-assemblies on liquid as well as solid surfaces.**

## 1. Introduction

2D or single-layer materials consisting of ultrathin films of one or few atomic or molecular layers with a crystalline structure present a broad range of unique properties, such as extremely high strength, electron mobility, thermal conductivity, remarkable optical characteristics, etc. 2D materials are thus the objects of extensive research aiming for applications in numerous domains such as flexible, nano- and optoelectronics, biomedicine, energy storage, and plasmonics.[1–3]

X-ray reflectivity (XRR) is vastly used to study surfaces and interfaces of hard and soft condensed matter materials, including 2D materials, nanomaterials, and biological systems. It allows deriving the laterally averaged electron density profile of a material surface region along its normal with sub-Angstrom precision.[4–6] This helps to determine various parameters including surface roughness, structures of a single layer or multilayered materials, and the effect of capillary waves on liquid surfaces. High-brilliance synchrotron X-ray beam allows resolving materials structure at molecular levels in real-time under environmental conditions, hardly accessible to other surface-sensitive experimental techniques.[7] Examples of such experiments are investigations of liquid surfaces and interfaces, using dedicated equipment and sample cells.[8–11] However, a particular issue exists related to the XRR from liquids. The wetting angle between the liquid and the support induces a curvature to the sample liquid, which generally complicates the data analysis.[12] This issue can be tackled by utilizing sample environments capable of working with large area samples, e.g., Langmuir trough,[13] applying special data treatment methods,[12,14] or using X-ray nanobeams.[15] However, in some cases, the sample curvature can be exploited advantageously, e.g., Festersen et al.[15] used a wide parallel synchrotron beam to record XRR curves in "one-shot" but limited in the range of scattering vector $q$.

The recent development of sample environments[16] dedicated to in situ and/or operando XRR studies opened new opportunities such as, e.g., the investigations of 2D materials during their growth on liquid metal catalysts (LMCats) by chemical vapor deposition (CVD).[17] These systems are promising for the growth of high-quality materials[18] but, at the same time, can be very demanding experimentally.[19] They must be adapted to high operation temperatures, high material evaporation, and exposure to a mixture of reactive gases at atmospheric pressure. In addition, they are confined to a limited-size sample

V. Belova, M. Jankowski, O. V. Konovalov
The European Synchrotron Radiation Facility – ESRF
71 Avenue des Martyrs
CS 40220, Grenoble Cedex 9 38043, France
E-mail: valentina.belova@esrf.fr; konovalo@esrf.fr
M. Saedi, I. M. N. Groot
Leiden Institute of Chemistry
Leiden University
P.O. Box 9502, Leiden 2300 RA, The Netherlands
G. Renaud
Univ. Grenoble Alpes
CEA
Grenoble IRIG/MEM/NRS 38000, France

The ORCID identification number(s) for the author(s) of this article can be found under https://doi.org/10.1002/admi.202300053.



**DOI: 10.1002/admi.202300053**

holder resulting in a significant wetting angle with the support, and they demand extreme surface sensitivity.[16,20] Despite all these difficulties, we have recently shown that in situ and real-time investigations of 2D materials on LMCats are now possible. Using synchrotron XRR, we resolved the structure of the liquid copper surface fully covered by floating single-layer graphene, which is a very weak X-ray scatterer.[20]

However, the growth kinetics of graphene on liquid copper is very complex, and different strategies for its growth result in different morphology evolution during growth.[20] That brings us to another technical challenge, which is the investigation of a patchy surface using XRR. Incomplete coverage of a surface with patches of another material with a lateral size smaller than the beam footprint on the surface (**Figure 1**a) results in an equivalent XRR curve of a film with a reduced electron density due to averaging over the illuminated area. The coverage may vary with time as in the case of single-atom-thick graphene crystals during their growth on liquid copper. Based on such a system, Figure 1b provides a simulation of the XRR curves of a patchy surface (graphene flakes) with a variable coverage ratio $X$, whereas Figure 1c shows these XRR curves normalized to the XRR curve of the substrate (liquid Cu, gray curve). The drop of the intensity around $q_z = 0.8$ Å$^{-1}$ is due to the Kiessig minimum, related to the height separation between the liquid surface and the graphene sheet.[12,21] Thus, one can see that the superposition of the signal from the covered and noncovered areas results in the loss of information.

Typically, the analysis of such patches with XRR is quite problematic unless supported by additional information obtained by diffuse off-specular scattering measurements or grazing incidence small angle X-ray scattering (GISAXS). However, these methods are applicable mainly for islands of nanometric size (up to a few micrometers in the best cases)[22,23] and are not sensitive to larger objects at the µm to mm scale. Imaging of a flat surface in XRR geometry using synchrotron X-rays cannot be applied directly because of the small beam size, usually below a few tens of µm, which has the same size on the detector plane after specular reflection (Figure 1a). This size is smaller than the pixel size of recent 2D photon-counting area detectors (Maxipix-ESRF: 55 µm, Eiger-Dectris: 75 µm, Pilatus-Dectris: 172 µm). To visualize the surface under the beam footprint, an optical element, i.e., a 2D X-ray lens, is needed after the sample to transform a bunch of parallel beams into a fan of diverging beams. The larger the obtained angular spread of the beam fan, the higher the magnification of the surface image. Compound refractive lenses (CRLs)[24,25] can be used to magnify the angular spread of the scattered beam.[26,27] An example of imaging in XRR geometry with an X-ray beam focused on the sample with 1D CRLs demonstrated the possibility of distinguishing if the surface under the beam was covered or not with a gold film.[28] However, due to the small refractive index of X-rays and the large number of CRLs needed, a long distance to the detector and a precise alignment of CRLs are required. Illumination of a flat sample by the narrow beam extended 1 cm in the direction perpendicular to the incidence plane ("pencil beam") and combined with the sample rotation around the normal to the sample surface provided surface tomography with a lateral resolution of 1.6 mm on a planar gold pattern sputtered on the silicon wafer.[29] Surface imaging can be achieved by scanning

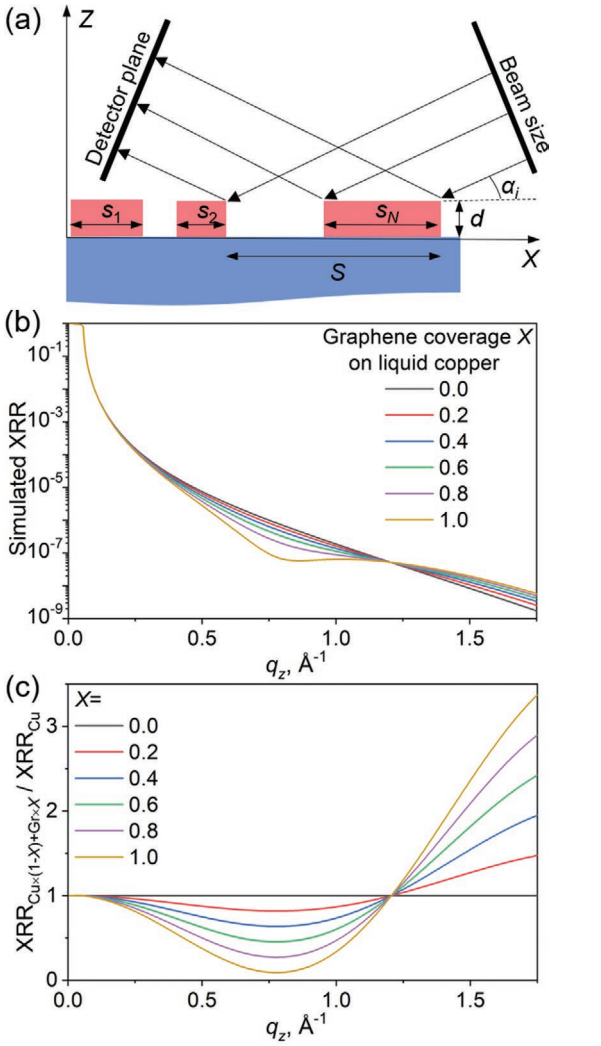


**Figure 1.** a) Example of a surface partially covered by another ultrathin material that forms patches of thickness $d$ and lateral sizes $s_i$ smaller than the angle-dependent beam footprint $S$. The coverage $X$ is $\sum s_i/S$. b) Simulated XRR reflectivity of such a patchy surface with different coverage $X$, where $X = 0$ is the bare substrate and $X = 1$ is full coverage. Patches are graphene crystals on liquid copper. c) The reflectivity curves from b) normalized to the theoretical XRR curve of bare liquid copper.

the sample under the microbeam at a fixed incident angle.[30] The resolution of these methods is limited by the size of the beam. Fine scanning is time-consuming, and measurement at a single incident angle does not bring information about the structure in the direction normal to the surface.

Here, we propose a development of the XRR technique that takes advantage of the sample curvature and thus allows to visualize patches of 2D materials during their growth on a curved surface, and ultimately to analyze the interfacial structure as a function of the domain size by employing CVD graphene on liquid Cu as a model system. Recently, we demonstrated that the curvature of the surface can be exploited in a positive manner allowing to perform XRR structural investigation during the growth. The method of XRR curve reconstruction upon measurements on spherically or cylindrically curved

surfaces with a curvature radius in the range from millimeters to meters was developed.[12] A curved sample surface naturally spreads the specularly reflected beam. Moreover, a smaller curvature radius results in a larger spread and, hence, larger image magnification. This can be used for surface imaging and, in the case of partial coverage of the surface with patches, for simultaneous measurement of XRR curves of the bare substrate and the substrate covered with a patch as the intensity of a reflected elementary ray depends on the surface density profile below it.

The work is organized as follows. First, we introduce the principle of the method. Then we demonstrate how the reflection signal on the detector depends on the graphene coverage on the liquid copper substrate. Next, we show that the spatially resolved XRR at a fixed incidence angle can be applied to follow the growth process in real time as an alternative to optical microscopy. Following the experimental results, we derive the interface parameters of the individual flakes such as their height on the metal substrate by splitting the conventional XRR scan into two components of the covered and noncovered areas. In the last subsection, we discuss the applicability of the presented method to other systems.

## 2. Results and Discussion

### 2.1. Method Principle

In this work, we elaborate the spatially-resolved XRR technique by considering the growth of graphene flakes on liquid Cu as a model system. In our previous works,[12,20] we presented in situ XRR measurements on bare liquid copper and liquid copper fully covered with a graphene layer grown by CVD at ≈1400 K, where $CH_4$ was used as the precursor gas in the mixture of $Ar/H_2$. Here, we use the data obtained during three different growth experiments: growth 1, growth 2, and growth 3, where the $CH_4/H_2$ ratio was $13\times10^{-3}$ (constant flow), $9\times10^{-3}$ (injection after accumulation for 30 s followed by a constant flow), and $13\times10^{-3}$ (injection after accumulation for 20 s followed by a constant flow), respectively. The videos of the growths recorded with an optical microscope and a digital camera are available in the Supporting Information. The typical curvature of the molten Cu drop in our experimental conditions is in the range of 0.1–0.3 m. The preparation time is long enough for the drop curvature to stabilize.

The schematic illustration of the X-ray beam reflection from a curved surface is provided in **Figure 2**a. The width of the spread on the detector $l$ depends on the sample curvature radius $R$, the incidence angle $\alpha_i$, and the sample-detector distance $L$. Let us consider two parallel rays impinging on a cylindrically curved surface. The first one, $r_{0,i}$, hits the apex of the surface at the $\alpha_i$ equal to the effective grazing angle of the beam. The second one, $r_{h,i}$, is separated by a distance $h$ (Figure 2b). After reflection on the spherically curved surface with the curvature radius $R$, they will propagate further as rays $r_{0,s}$ and $r_{h,s}$, respectively, with an angular separation $2\Delta\alpha_{i,h}$. Here $\Delta\alpha_{i,h}$ is the difference between the grazing angles of two rays $r_{0,i}$ and $r_{h,i}$, and can be calculated, following Konovalov et al.[12] as

$$\Delta\alpha_{i,h} = \arccos\left(\frac{h}{R}+\cos\alpha_i\right)-\alpha_i \tag{1}$$

The magnification is as large as the ratio between the width of the beam spread on the detector $l$ and the beam footprint on the surface $S$.

Note that the spread of the reflected beam in the direction perpendicular to the plane made by the incident beam and the beam that a flat surface would reflect is a few orders of magnitude smaller than the spread in this plane, along the exit angle direction. As a result, the complex 2D description can be safely reduced to 1D, and only one direction of the 2D detector is considered: that which the specular reflection would give from a flat surface. The general case of a 3D curved surface can thus be reduced to that of a cylinder with an incident beam perpendicular to its axis.[14]

### 2.2. Reflection Signal on Detector at Fixed Incidence Angle

In the case of uniform coverage, whether it is bare copper or copper covered with a complete graphene layer, for any

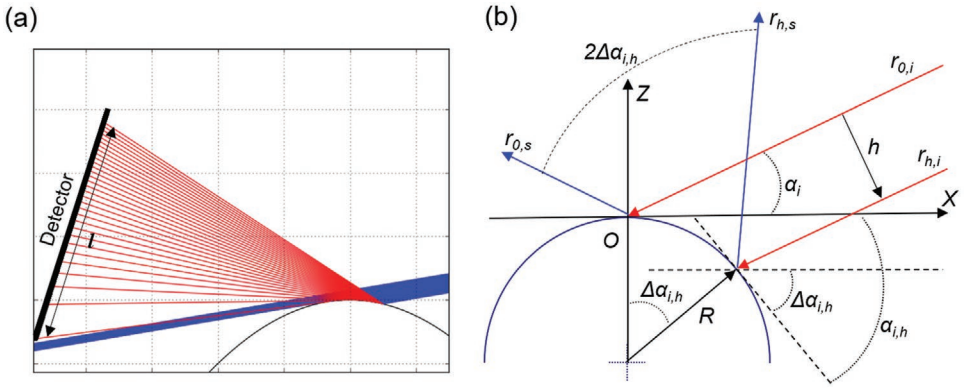


**Figure 2.** a) Illustration of the angular spread of the collimated X-ray beam (blue) reflected by a cylindrical surface. Narrow red lines represent elementary rays. $l$ is the spread width on the detector. b) Detailed scheme where the incident beam, coming from the right side, propagates in the plane $XOZ$ normal to the axis of a cylinder with a radius $R$ that is perpendicular to the figure plane. $h$ is the offset of the elementary ray $r_{h,i}$ from the beam center $r_{0,i}$. The angle $\alpha_i$ is the effective grazing angle, while $\alpha_{i,h}$ and $\Delta\alpha_{i,h}$ are the actual grazing angle of $r_{h,i}$ and the difference of this angle from $\alpha_i$, respectively.

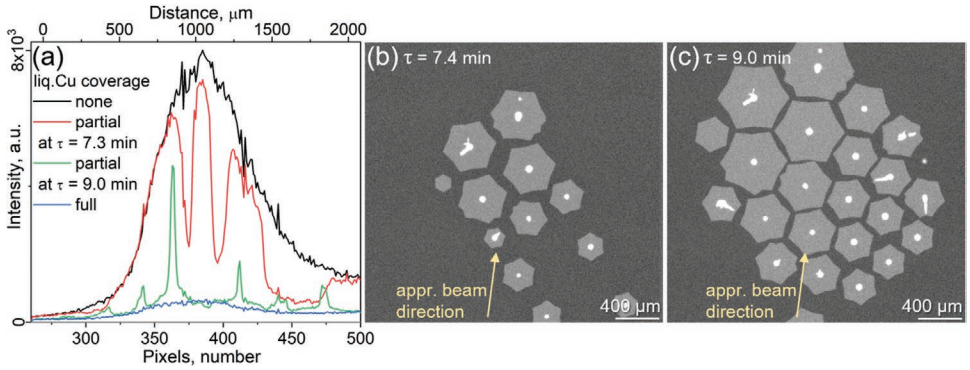


**Figure 3.** a) XRR intensity of the reflected beam measured on the detector along its vertical axis, for $\alpha_i = 2.05°$ and $q_z = 0.8$ Å$^{-1}$ during the CVD growth of graphene (growth 1). The black curve corresponds to the bare Cu surface. The red one corresponds to the partially covered surface after 7.4 min since the $CH_4$ valve was open. The green one corresponds to the partial coverage after 9.0 min of $CH_4$ exposure. The blue one corresponds to the full coverage by graphene of the surface under the beam. The double *x*-axis corresponds to the pixel number (on the bottom) and the distance within the footprint on the sample (on the top). b,c) The corresponding microscopy images for the red (7.4 min, b) and green (9 min, c) curves, respectively. The yellow arrow indicates the approximate direction of the incident beam.

effective grazing angle $\alpha_i$, the reflected beam intensity profile on the detector plane in the vertical direction has a wide smooth "bell"-like shape (**Figure 3**a, black and blue curves) caused by the spread of the beam (Figure 2a). The scattering curves presented in Figure 3a were obtained during growth 1 at a grazing angle $\alpha_i$ value of 2.05°, which corresponds to a scattering vector $q_z = 0.8$ Å$^{-1}$. The black curve in Figure 3a is obtained on the bare liquid copper before the CVD growth of the graphene layer, and the blue curve is measured at the end of the growth when a graphene film of atomic thickness fully covers the surface under the beam. Following the calculations shown in Figure 1c, one can see that at $q_z = 0.8$ Å$^{-1}$ the scattering intensity from the liquid copper covered with a uniform layer of graphene is about one order of magnitude lower than the scattering from the bare liquid surface. The reason is that this position on the XRR curve is close to the minimum of the first Kiessig fringe (itself related to the height of the graphene layer above the liquid copper).[12,20,21,31] This intensity contrast originating from the Kiessig oscillations helps to distinguish between the covered and noncovered parts of the surface.

The red and green curves in Figure 3a are obtained consequently at different times of the growth (7.4 and 9.0 min after opening the $CH_4$ valve, respectively), resulting in partial coverage of the copper surface with graphene flakes. The growth coverage was monitored in real time with radiation-mode optical microscopy.[20] The microscopy images in Figure 3b,c were taken at 7.4 and 9.0 min after opening the $CH_4$ valve, and the start of the growth, corresponding to the red and green curves. The scattering profile of the surface with partial coverage varies between the two extreme cases of a bare and a fully covered surface. At the earlier growth stage, when graphene crystal flakes are small relative to the beam footprint and the distance between them is larger (Figure 3b), the major part of the scattering intensity (Figure 3a, red curve) is defined by the scattering from the bare surface, where are only four intervals where the scattering intensity drops as four graphene flakes (at pixels 307, 374, 398, and 453) pass under the beam. With time, as $CH_4$ continues to flow, the number of flakes and their size increase (Figure 3c). Consequently, the scattering contribution from graphene begins to dominate the detector profile (Figure 3a, green curve), and thus, we see peaks of higher intensity corresponding to the regions with bare copper between graphene flakes. However, we should be careful when interpreting these data due to some possible interference effects. For example, the white centers of the flakes, most likely multilayer carbon layers stacks that get etched away at later growth stages,[20] also introduce regions of higher intensity, as can be seen: at pixels 340 and 442 on the green curve.

### 2.3. Time-Resolved Growth Monitoring with XRR and Optical Microscopy

While Figure 3a presents the reflected signal at a few selected moments of growth 1, the 2D map in **Figure 4**a shows the time scan (*y*-axis) of the scattering on the detector (*x*-axis) during the whole duration of growth 1: starting from bare liquid copper (areas of higher intensity) and finishing when the graphene layer is complete. The upper limit of the time resolution is defined by the detector readout frame rate (280 Hz for Maxipix, in our case). The image visualizes the movement and growth of the graphene crystals (areas of lower intensity), which, ≈27 min after the introduction of $CH_4$ flow, occupy the entire surface under the beam. Information about the graphene crystals' size, inter-flake distances, and kinetics can be extracted since the distances in pixels on the detector can be correlated with real-space objects on the sample surface. For example, the length *S* of the beam footprint on the curved sample at $\alpha_i$ can be found as

$$S = 2R \arcsin\left(\frac{W}{2R\sin\alpha_i}\right) \tag{2}$$

where *W* is the beam size in the scattering plane. The spread width on the detector *l* in the vertical direction (plane *XOZ*, Figure 2b) can be derived as

$$l = 2L\tan\frac{S}{R} + W \tag{3}$$

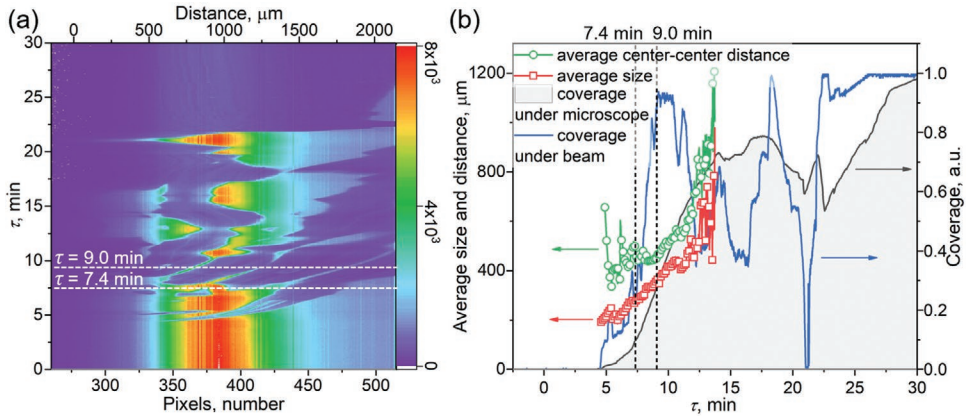


**Figure 4.** a) Time-scan of the scattering signal on the detector in the vertical direction during the CVD graphene growth (growth 1). The color scale of the intensity is linear. The vertical axis represents the time after the opening of the $CH_4$ valve, and the horizontal axis is (bottom) the pixel number of the detector (along the reflected beam fan) and (top) the corresponding distance within the footprint on the sample. The regions of higher intensity correspond to the bare liquid Cu surface. The intensity is minimum when the surface is covered by graphene. The dashed lines indicate the points of 7.4 and 9.0 min, corresponding to the profiles in Figure 3a. b) Quantitative analysis of the growth 1: average flake lateral size (red) and average center-to-center distance between neighboring flakes (green) deduced by optical microscopy, time-evolution of the layer coverage under the microscope (gray) and under the X-ray beam, extracted from the image a) (blue).

where $L$ is the sample-detector distance.

Typically, the X-ray beam has the highest intensity in the center and its shape can be fitted with a Gaussian. Thus, the beam size is characterized by the full width at half maximum (FWHM) in vertical and horizontal directions, which in our case is 22 × 10 μm. The intensity profile of the reflected beam on the detector, such as the one in Figure 2a (black curve), can also be fitted with a Gaussian. Here, we get an FWHM of ≈70 pixels. Using a pixel size of 55 μm, we derive $l$ = 3.85 mm. With $L$ = 488.4 mm and $\alpha_i$ = 2.05°, and applying Equations (2) and (3), we find $R$ = 157 mm and $S$ = 615 μm. Consequently, a pixel of the detector corresponds to the distance of ≈9 μm at the sample surface. This ratio is applied to the top $x$-axis of Figures 3a and 4a, thus helping to correlate the intensity drops with the flakes' movement on the liquid Cu surface. At these conditions, the samples with larger $R$ can be used as well, e.g., up to $R$ = 500 mm, which would result in a magnification factor of 2. The $R$ defined via the spread $l$ is related to the local curvature of the surface and is not necessarily constant for the entire drop. We also note that we do not observe a change in the $R$ between the bare and fully covered states within a single measurement (30 min). It is also possible to deduce the coverage ratio under the beam by dividing the data in Figure 4a into two components: covered and noncovered areas, the resulting time-evolution is shown in Figure 4b (blue).

The graph in Figure 4b also presents the analysis of the optical microscopy images recorded during growth 1 in parallel with the X-ray measurements, see Video Growth_S1 (Supporting Information). We use MATLAB to extract the following parameters: the lateral size of the flakes (red), the center-to-center distances between the neighboring flakes (green), and the surface coverage with graphene in the field of view (gray). The area of the sample accessible with the optical microscope through the glass window is ≈5.0 × 3.7 mm, which is much larger than the beam footprint. Therefore, this technique provides a larger data set. However, since the early growth stages occur in the center (vertex) of the liquid Cu drop where the beam is aligned, the data from both methods can be correlated.

Comparing both plots in Figure 4, we can see that the first flake appears after 4 min of exposure to methane, then the number of flakes increases. At time $\tau$ = 9 min, the densest packing of the flake assembly is observed while the flakes' size is the order of a few hundred μm. Then due to the strong interactions between the flakes leading to their coalescence, they begin to move, opening up the copper surface at $\tau$ = 20–23 min. The center of the sample (part under the beam) is entirely covered by graphene after 27 min, while there are still some empty areas closer to the sample edges (Video Growth_S1, Supporting Information).

### 2.4. Reconstruction and Fitting of XRR Curves from Partially-Covered Surface

The simultaneous and disentangled presence of the specular reflection from the bare and graphene-covered surface can be used to measure the two corresponding XRR curves with one single conventional $\alpha_i$–$2\alpha_i$ angular scan. In our previous work,[20,21] we characterized the height of the graphene on Cu, also called the "gap" between the surface of the liquid catalyst and the graphene layer fully covering the surface, as this parameter is related to the interlayer van der Waals binding force between the metal and the carbon layer. However, it is unknown whether the gap value is identical for isolated flakes of graphene. Therefore, we address this aspect in the following experiment.

**Figure 5** presents $\alpha_i$–$2\alpha_i$ angular measurements of the X-ray reflection on a spherically curved surface partially covered with graphene flakes during two different growth experiments: growth 2 and growth 3. Plots with the average flake size during the growths, followed by optical microscopy, are provided in Figure S1 based on Videos Growth_S2 and Growth_S3 (Supporting Information). In growth 2, the flakes are generally smaller and reach a size of 0.3 mm when the reflectivity

ADVANCED MATERIALS INTERFACES
Open Access
www.advmatinterfaces.de

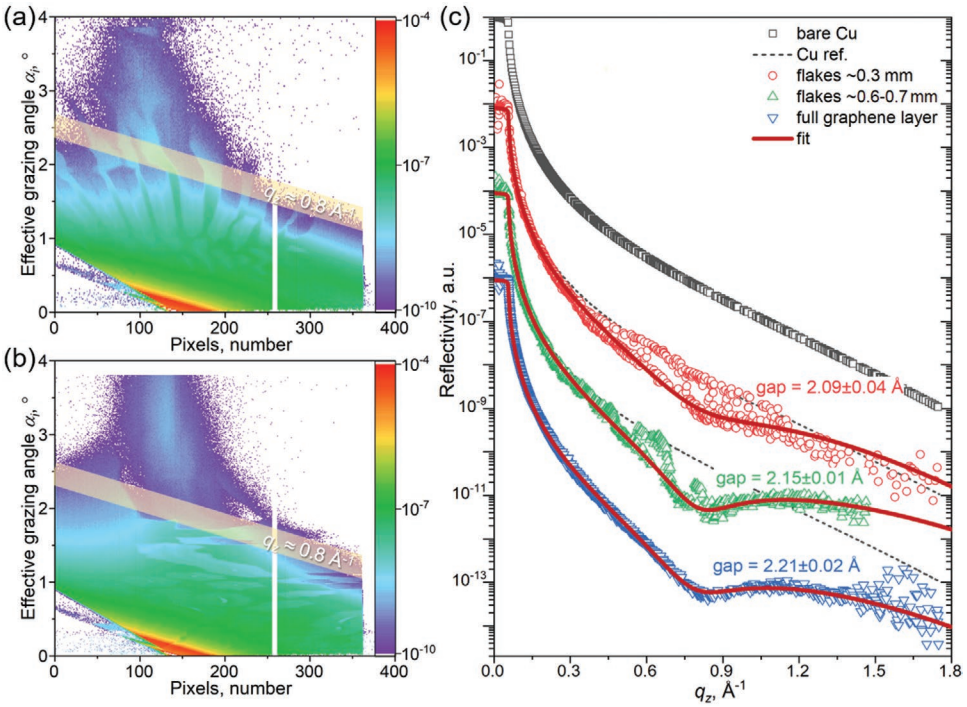


**Figure 5.** a,b) 2D maps of the XRR signal on the detector (horizontal axis shows the detector pixels along the spread of the reflected beam) for a set of effective incident grazing angles (vertical axis) recorded during the CVD growth of graphene with the presence of flakes of different sizes: a) growth 2 with flakes of 0.3 mm, b) growth 3 with flakes of 0.6–0.7 mm in the lateral dimension when passing through the Kiessig minimum at $q_z = 0.8$ Å$^{-1}$ (highlighted in yellow). The color scale of the intensity is logarithmic. c) XRR curves of bare Cu (gray), of the surface during growth 2 with smaller flakes reconstructed from the 2D map in (a) (red), of the surface during growth 3 with larger flakes reconstructed from the 2D map in (b) (green), and of the sample fully covered with graphene (blue). The fit corresponds to the graphene/Cu part of the curves. The curves are vertically offset for clarity. The gray dashed line is the shifted XRR curve of bare Cu introduced to emphasize the splitting of the red and green curves into two components.

measurement reaches the Kiessig minimum at $\alpha_i = 2.05°$ (as the most important part of the XRR curve for the fitting), whereas for growth 3 the flakes are larger reaching 0.6–0.7 mm in size at the same scanning point. These figures are built accordingly to the method described by Konovalov et al.[12] The horizontal axis is the position on the effective 1D detector. The vertical axis is the effective grazing angle. Color codes correspond to the absolute scattering intensity. The width of the beam spread on the detector decreases with the increase of the $\alpha_i$. Similar to Figure 4a, in Figure 5a,b we see areas corresponding to the reflection from the covered and noncovered parts of the surface, movement, and growth of graphene crystals. Each point on the map in Figure 5a,b corresponds to a specific scattering vector. The yellow marker highlights the area around $q_z = 0.8$ Å$^{-1}$. After assigning each pixel of these 2D images to the correct $q_z$ values, the conventional 1D XRR curves can be reconstructed[12] with the points belonging either to the XRR of the bare liquid copper or the XRR of the surface covered with graphene (Figure 4c). For clarity, we consider only the central part of the beam with the highest intensity (the half of the FWHM) during the reconstruction to minimize any parasitic scattering. The splitting of the XRR curves into two components is more pronounced in the case of the smaller flakes (red curve), while in the case of the green curve, a flake larger than the footprint covers the surface under the beam as the scan passes through the Kiessig minimum (Figure 4b; and Video Growth_S3, Supporting Information).

The red and green curves in Figure 5c are obtained from the measurement during growths 2 and 3 presented in Figure 5a,b. The inclusion of points from either covered or bare parts of the copper surface results in partial splitting of the XRR curves. To illustrate that the measured points belong to two different states of the sample's surface, XRR curves measured with the same approach for bare liquid copper (gray) and the copper entirely covered with graphene (blue) are also shown in Figure 5c. As we can see, the described method allows obtaining two XRR curves corresponding to two coexisting states of the system.

The part of the XRR curves belonging to the graphene/Cu (excluding the points belonging to bare Cu) was fitted with a slab model using the Refl1D software.[32] The slabs include Cu (bulk), C (single atomic layer), and a void in between.[12,20,21] The fitting parameters are combined in **Table 1**. We define the interlayer Cu-C gap as the distance between the inflection point of the Cu slab and the center of the C layer, i.e., $d_{void} + d_{Gr}/2$, where $d_{void}$ is the thickness of the void and $d_{Gr}$ is the thickness of the graphene layer (C atomic radius) as illustrated in Figure S2 (Supporting Information). As we can assume from the fit results, the gap can be somewhat smaller for individual flakes: 2.09 ± 0.04 Å in the case of 0.3 mm flakes (the average size at the time when the scattering angle is around the Kiessig minimum at 0.8 Å$^{-1}$), 2.15 ± 0.01 Å in the case of 0.6–0.7 mm flakes, and 2.21 ± 0.02 Å for the complete layer. The decrease of the separation by ≈6% for small flakes with respect to the continuous layer can be argued to be caused by the supposedly

**Table 1.** Fitting parameters extracted from the XRR curves of the flakes and the complete graphene layer. The Cu density, $\rho_{Cu}$, and the graphene density, $\rho_{Gr}$, are fixed, as well as the thickness of the carbon layer (atomic radius of C), $d_{Gr}$. The other parameters, $\sigma_{Cu}$ and $\sigma_{Gr}$, roughness of liquid Cu and the carbon layer, and $d_{void}$, the width of the void between Cu and C slabs, are fitted. The 95% confidence intervals of the fit are indicated.

| | $\rho_{Cu}$ [g cm$^{-3}$] | $\sigma_{Cu}$ [Å] | $\rho_{Gr}$ [g cm$^{-3}$] | $d_{Gr}$ [Å] | $\sigma_{Gr}$ [Å] | $d_{void}$ [Å] |
|---|---|---|---|---|---|---|
| Flakes ≈0.3 mm | $7.96_{(fixed)}$[34] | 1.08 ± 0.05 | $5.36_{(fixed)}$[35] | $1.42_{(fixed)}$[36] | 1.44 ± 0.06 | 1.38 ± 0.04 |
| Flakes ≈0.6–0.7 mm | | 0.90 ± 0.01 | | | 0.93 ± 0.01 | 1.44 ± 0.01 |
| Complete layer | | 0.97 ± 0.02 | | | 1.05 ± 0.02 | 1.50 ± 0.02 |

stronger interaction of the liquid metal substrate with the individual flakes. Indeed, the C atoms at the edges of the flakes "miss" C neighbors. They tend to share electrons with Cu, thus "chemically" binding to it, as opposed to the center of the flakes that undergo physisorption through van der Waals interactions. The resulting flakes are bent near the edges with edge C atoms being much closer to Cu than for an infinite layer. This also applies some stress to the center of the flake that moves slightly toward the underlying Cu surface. Indeed, for extremely small flakes, atomistic simulations predict the C-clusters to sink slightly into the Cu surface.[33] The much larger value of the equivalent roughness of graphene in the case of smaller flakes might indicate the presence of a much larger dispersion of Cu-to-C distances. However, we note that the mentioned error bars indicate the 95% confidence intervals of the fit itself, whereas we estimate the total experimental error bar of the Cu-C gap as ± 0.05–0.10 Å based on the reproducibility. Thus, although our results show a trend toward a shorter distance for small flakes with respect to the infinite layer, the exact value should be treated with caution.

### 2.5. Applicability to Other Systems

In this section, we evaluate the potential applicability of the proposed approach to other systems. Note first that curved surfaces can be formed naturally due to the surface tension of a liquid state and can be forced mechanically or intentionally fabricated in the case of a solid substrate. Therefore, the curvature of the surface is expected to vary widely between different systems, as is, of course, the reflected intensity contrast.

A suitable experimental system should meet a few criteria.

First, the substrate should have a curvature at least in one direction, along the measurement axis. The curvature radius $R$ should preferably be in a range between 10 and 500 mm. A smaller $R$ is an advantage for the resolution but would result in implementation problems and the loss of part of the scattered beam, while for a larger $R$, the spatial resolution of different surface states becomes very limited. However, for a large $R$, the magnification/resolution can be improved to a certain extent by decreasing the incidence angle and increasing the sample-detector distance. The former would increase the angular spread between two neighboring reflected elementary rays and the latter would increase the spatial separation of these two rays on the detector plane (Figure 2).

Next, for the visualization function to be effective, it is sufficient to have a contrast in the scattered intensity between the covered and noncovered areas within some part of the accessible $q_z$ range. The presence of a slab of finite thickness on top of a substrate with different electron density ensures the appearance of Kiessig oscillations,[31] and the reflectivity contrast is defined by the difference in the electron density between these two materials. Let us consider a typical system consisting of an organic layer with a typical density of 0.8 g cm$^{-3}$ (mainly consisting of hydrocarbon chains $(CH_2)_n$) covering a solid substrate, e.g., muscovite mica, or a liquid substrate, e.g., water. We get two pairs of XRR curves with different contrast as demonstrated in **Figure 6**. In the case of mica, the reflected intensity of the surface covered with a film is 6.5 times lower at the minima than that of the bare substrate. For a water substrate, the contrast is 2.5 times, which is low but still sufficient for image construction. This last example shows that the method is applicable even when the electronic density contrast is only 20%. In general, the scattering intensity contrast has to be larger than the statistical noise level of measured values. The maximum contrast for the Kiessig oscillations can be obtained when the film density is half that of the substrate, as can be deduced from the master formula of the kinematical reflectivity.[37]

The third requirement to bear in mind is that the investigated patches should have the same thickness, whereas the thickness itself or/and the number of layers is not of importance as long as the oscillation period can be resolved. The presence of patches of different thicknesses would result in a different XRR pattern for each of them, and their superposition within a single image would smear out the contrast and largely entangle the interpretation.

With these conditions, we suggest that the approach presented here has great potential to study the growth and self-assembly processes on liquid surfaces in soft matter systems such as, e.g., colloidal crystals,[38] liquid crystals,[39] Gibbs and Langmuir monolayers, proteins and peptides,[40] and electrochemically induced growth of ultrathin crystalline layers at liquid–liquid interfaces.[41] It can also be used to analyze the deposition of thin films or 2D materials, layer-by-layer self-assembly, and molecule adsorption, on liquids and solid substrates, given that the substrate surface has curvature.[14,42,43]

## 3. Conclusion

In this work, we have implemented a convex surface to perform a spatially resolved X-ray reflectivity. This allows imaging the surface along one direction and provides qualitative information on the size, separation distance, and coverage of the typical

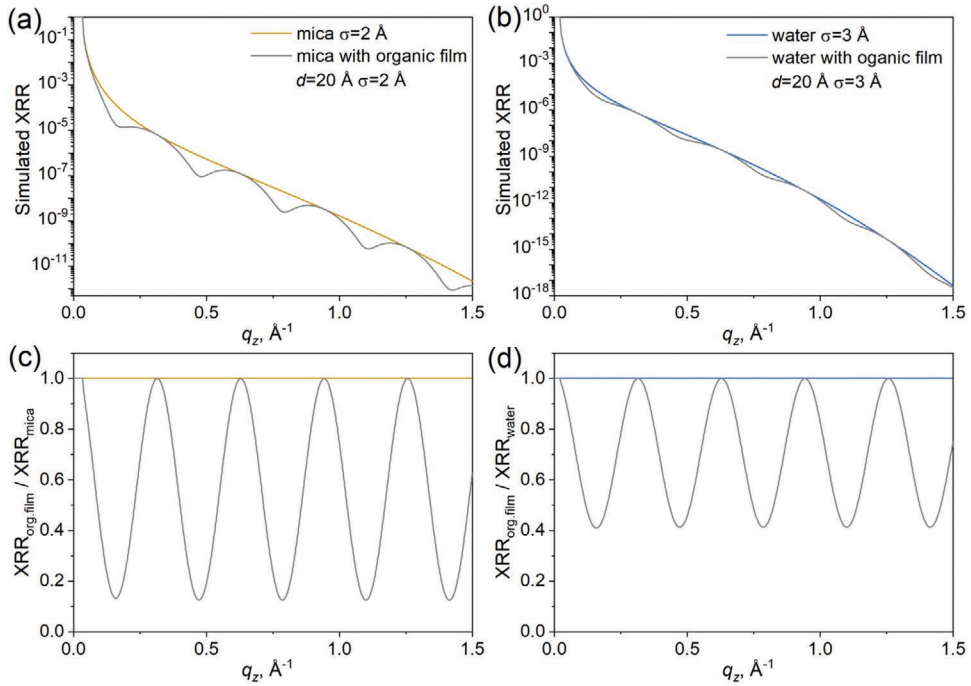


**Figure 6.** Top: simulated XRR curves for a hypothetical system consisting of an organic film ($(CH_2)_n$) with density $\rho$ of 0.8 g cm$^{-3}$ on a typical solid a) or liquid b) substrate—mica and water, respectively. The other simulation parameters (thickness $d$ and roughness $\sigma$) are placed in the legend. Bottom: XRR curves from a) and b) normalized to the XRR curves of the bare substrates, in the case of mica c) and water d) illustrating the intensity contrast defined by the Kiessig oscillations.

features of an inhomogeneously covered surface. Moreover, we can distinguish and quantitatively recover the individual X-ray reflectivity curves from different surface points, and thus deduce their electron density profiles perpendicular to the surface. The length probed along the beam depends on the incident angle and can thus be varied between 100 µm to a few mm. The typical spatial resolution of the technique is ≈micrometer. The high data acquisition rate allows real-time monitoring of system kinetics with ≈millisecond time resolution

As a model system, this new method was implemented to monitor the growth of single-layer graphene flakes on liquid copper in real time. The method was enabled by the naturally curved surface of the small liquid drop, which previously used to be regarded as a nuisance in standard XRR experiments. The results were compared to the now well-established method of radiation-mode optical microscopy. The reconstruction of the XRR curves from both covered and noncovered parts of the surface allows deducing the flake height/separation gap on the substrate at different stages of the growth, corresponding to different average flake sizes.

This 1D "imaging" technique through XRR could be extended to a 2D visualization of the sample by using a much wider beam in the direction parallel to the sample. Then the information in the direction perpendicular to the incident beam would be recorded along the corresponding direction of the detector, which is presently not exploited. The technique opens the perspective for the development of XRR-based hyperspectral imaging (or microscopy) that would allow recording an XRR spectrum for every point on a microscopic 2D surface following the generation of a magnified 2D image, where each pixel correlates to a physical/chemical parameter at that point on the surface (e.g., materials type, number of layers, separation gap).

## 4. Experimental Section

XRR measurements on a liquid surface using a double crystal deflector (DCD)[11] were performed at the ESRF beamline ID10 using a monochromatic X-ray beam of 22 keV energy. The beam size on the sample position was 10 × 22 µm$^2$ (HxV, the FWHMs of Gaussian shapes). The scattered X-ray beam was measured with a Maxipix 2D photon-counting pixel detector with 1 mm thick CdTe sensors, pixel size 55 × 55 µm$^2$, and a detector area: of 28.4 × 28.4 mm$^2$. The XRR measurements on bare liquid copper and the copper surface covered with the CVD-grown graphene layer were performed in situ at 1400 K and 200 mbar in a reactor for CVD growth on a liquid metal catalyst.[16] The reactor was designed and customized especially for real-time in situ X-ray reflectivity and diffraction measurements with the incident and exit grazing angles of –1° to +22°. The use of a wide cylindrical Be window, transparent to hard X-rays, and the reduced gas pressure allow for minimizing the beam attenuation and the scattering from the gas molecules. The thin copper layer and its excellent heat conduction minimize the temperature differences and hence the convection inside the liquid layer. Thanks to low-pressure CVD gas and its low flow rate, drifting due to gas flow is also negligible. The vibration isolation system below the sample holder and the double crystal deflector design of the diffractometer also reduce the mechanical disturbance of liquid the metal. Methane gas diluted in Ar was used as a precursor and the $CH_4/H_2$ ratio was 13 × 10$^{-3}$ (constant flow), 9 × 10$^{-3}$ (injection after accumulation for 30 s followed by a constant flow), and 13 × 10$^{-3}$ (injection after accumulation for 20 s followed by a constant flow) for growths 1, 2, and 3, respectively. More details on the growth conditions of the single-atom-high graphene layer are described in ref. [20].

## Supporting Information

Supporting Information is available from the Wiley Online Library or from the author.

## Acknowledgements

The authors acknowledged the European Synchrotron Radiation Facility for the provision of synchrotron radiation facilities and the use of the surface scattering end-station at beamline ID10. The authors thanked European Union's Horizon 2020 research and innovation program under Grant Agreement No. 951943 (DirectSepa) for funding.

## Conflict of Interest

The authors declare no conflict of interest.

## Data Availability Statement

The data that support the findings of this study are available from the corresponding author upon reasonable request.

## Keywords

2D materials, curved surfaces, graphene, imaging, liquid surfaces, synchrotron radiation, X-ray reflectivity

Received: January 21, 2023
Revised: March 10, 2023
Published online:

[1] K. Khan, A. K. Tareen, M. Aslam, R. Wang, Y. Zhang, A. Mahmood, Z. Ouyang, H. Zhang, Z. Guo, *J. Mater. Chem. C* **2020**, *8*, 387.
[2] Z. Xiong, L. Zhong, H. Wang, X. Li, *Materials* **2021**, *14*, 1192.
[3] P. Ares, K. S. Novoselov, *Nano Mater. Sci.* **2022**, *4*, 3.
[4] E. Chason, T. M. Mayer, *Crit. Rev. Solid State Mater. Sci.* **1997**, *22*, 1.
[5] J. Daillant, A. Gibaud, *X-Ray and Neutron Reflectivity: Principles and Applications*, Springer, Heidelberg **1999**.
[6] M. Tolan, *X-Ray Scattering from Soft-Matter Thin Films: Materials Science and Basic Research*, Springer, Heidelberg **1999**.
[7] M. Jankowski, V. Belova, Y. Chushkin, F. Zontone, M. Levantino, T. Narayanan, O. Konovalov, A. Pastore, *Nucl. Instrum. Methods Phys. Res., B* **2023**, *538*, 164.
[8] V. Honkimäki, H. Reichert, J. S. Okasinski, H. Dosch, *J. Synchrotron. Radiat.* **2006**, *13*, 426.
[9] T. Arnold, C. Nicklin, J. Rawle, J. Sutter, T. Bates, B. Nutter, G. McIntyre, M. Burt, *J. Synchrotron. Radiat.* **2012**, *19*, 408.
[10] B. M. Murphy, M. Greve, B. Runge, C. T. Koops, A. Elsen, J. Stettner, O. H. Seeck, O. M. Magnussen, *J. Synchrotron. Radiat.* **2014**, *21*, 45.
[11] O. Konovalov, V. Belova, M. Saedi, I. Groot, G. Renaud, M. Jankowski, preprint arXiv:2210.12827 **2022**.
[12] O. V. Konovalov, V. Belova, F. L. Porta, M. Saedi, I. M. N. Groot, G. Renaud, I. Snigireva, A. Snigirev, M. Voevodina, C. Shen, A. Sartori, B. M. Murphy, M. Jankowski, *J. Synchrotron. Radiat.* **2022**, *29*, 711.
[13] W. B. Yun, J. M. Bloch, *Rev. Sci. Instrum.* **1989**, *60*, 214.
[14] W. H. Briscoe, F. Speranza, P. Li, O. Konovalov, L. Bouchenoire, J. Van Stam, J. Klein, R. M. J. Jacobs, R. K. Thomas, *Soft Matter* **2012**, *8*, 5055.
[15] S. Festersen, S. B. Hrkac, C. T. Koops, B. Runge, T. Dane, B. M. Murphy, O. M. Magnussen, *J. Synchrotron. Radiat.* **2018**, *25*, 432.
[16] M. Saedi, J. M. De Voogd, A. Sjardin, A. Manikas, C. Galiotis, M. Jankowski, G. Renaud, F. L. Porta, O. Konovalov, G. J. C. Van Baarle, I. M. N. Groot, *Rev. Sci. Instrum.* **2020**, *91*, 013907.
[17] C. Tsakonas, M. Dimitropoulos, A. C. Manikas, C. Galiotis, *Nanoscale* **2021**, *13*, 3346.
[18] P. Aukarasereenont, A. Goff, C. K. Nguyen, C. F. McConville, A. Elbourne, A. Zavabeti, T. Daeneke, *Chem. Soc. Rev.* **2022**, *51*, 1253.
[19] Y. Ding, H. Shi, M. Zeng, L. Fu, *Adv. Funct. Mater.* **2022**, *32*, 2202469.
[20] M. Jankowski, M. Saedi, F. La Porta, A. C. Manikas, C. Tsakonas, J. S. Cingolani, M. Andersen, M. De Voogd, G. J. C. Van Baarle, K. Reuter, C. Galiotis, G. Renaud, O. V. Konovalov, I. M. N. Groot, *ACS Nano* **2021**, *15*, 9638.
[21] H. Gao, V. Belova, F. La Porta, J. S. Cingolani, M. Andersen, M. Saedi, O. V. Konovalov, M. Jankowski, H. H. Heenen, I. M. N. Groot, G. Renaud, K. Reuter, *Adv. Sci.* **2022**, *9*, 2204684.
[22] S. K. Sinha, Y. P. Feng, C. A. Melendres, D. D. Lee, T. P. Russell, S. K. Satija, E. B. Sirota, M. K. Sanyal, *Physica A* **1996**, *231*, 99.
[23] I. A. Vartanyants, D. Grigoriev, A. V. Zozulya, *Thin Solid Films* **2007**, *515*, 5546.
[24] A. Snigirev, V. Kohn, I. Snigireva, B. Lengeler, *Nature* **1996**, *384*, 49.
[25] B. Lengeler, C. Schroer, J. Tümmler, B. Benner, M. Richwin, A. Snigirev, I. Snigireva, M. Drakopoulos, *J. Synchrotron. Radiat.* **1999**, *6*, 1153.
[26] T. Roth, C. Detlefs, I. Snigireva, A. Snigirev, *Opt. Commun.* **2015**, *340*, 33.
[27] H. Simons, A. King, W. Ludwig, C. Detlefs, W. Pantleon, S. Schmidt, F. Stöhr, I. Snigireva, A. Snigirev, H. F. Poulsen, *Nat. Commun.* **2015**, *6*, 6098.
[28] S. Lyatun, D. Zverev, P. Ershov, I. Lyatun, O. Konovalov, I. Snigireva, A. Snigirev, *J. Synchrotron. Radiat.* **2019**, *26*, 1572.
[29] V. A. Innis-Samson, M. Mizusawa, K. Sakurai, *Anal. Chem.* **2011**, *83*, 7600.
[30] K. Sakurai, M. Mizusawa, M. Ishii, S. I. Kobayashi, Y. Imai, *J. Phys. Conf. Ser.* **2007**, *83*, 012001.
[31] H. Kiessig, *Ann. Phys.* **1931**, *5*, 769.
[32] P. A. Kienzle, J. Krycka, N. Patel, I. Sahin, Refl1D (Version 0.8.15) [Computer Software], University of Maryland, College Park, MD Retrieved Oct 31, **2022**.
[33] M. Andersen, J. S. Cingolani, K. Reuter, *J. Phys. Chem. C* **2019**, *123*, 22299.
[34] M. J. Assael, A. E. Kalyva, K. D. Antoniadis, R. Michael Banish, I. Egry, J. Wu, E. Kaschnitz, W. A. Wakeham, *J. Phys. Chem. Ref. Data* **2010**, *39*, 033105.
[35] A. I. Savvatimskiy, *Carbon* **2005**, *43*, 1115.
[36] L. Pauling, *The Nature of the Chemical Bond and the Structure of Molecules and Crystals: An Introduction to Modern Structural Chemistry*, Cornell University Press, Ithaca, NY **1960**.
[37] J. Als-Nielsen, D. McMorrow, *Elements of Modern X-Ray Physics*, Wiley, London **2011**.
[38] G. Meng, J. Paulose, D. R. Nelson, V. N. Manoharan, *Science* **2014**, *343*, 634.
[39] P. Popov, E. K. Mann, A. Jákli, *J. Mater. Chem. B* **2017**, *5*, 5061.
[40] X. Zhang, C. Gong, O. U. Akakuru, Z. Su, A. Wu, G. Wei, *Chem. Soc. Rev.* **2019**, *48*, 5564.
[41] A. Sartori, R. P. Giri, H. Fujii, S. C. Hövelmann, J. E. Warias, P. Jordt, C. Shen, B. M. Murphy, O. M. Magnussen, *Nat. Commun.* **2022**, *13*, 5421.
[42] F. Sun, W. Cai, Y. Li, L. Jia, F. Lu, *Adv. Mater.* **2005**, *17*, 2872.
[43] L. Ma, X. Liu, A. K. Soh, L. He, C. Wu, Y. Ni, *Soft Matter* **2019**, *15*, 4391.